Rift Focusing and Magmatism During Late-Stage Rifting in Afar

C. Moore[1] , T. J. Wright[1] , and A. Hooper[1]

[1]COMET, School of Earth and Environment, University of Leeds, Leeds, UK

Abstract Processes that facilitate the transition between continental rifting and sea-floor spreading remain unclear. Variations in the spatial distribution of extension and magmatism through Afar and into the Red Sea are indicative of temporal evolution of the rifting process. We develop a time series of Sentinel-1 interferometric synthetic aperture radar (InSAR) observations of ground deformation covering the whole Afar rift zone from 2014 to 2019, to study the distribution of extension. By incorporating Global Navigation Satellite System observations, we resolve 3D average velocities in the vertical, rift-perpendicular, and rift-parallel directions. Results show the spatial distribution of long-wavelength deformation over the rift zone, as well as deformation at individual volcanic centers, including Dallol, Nabro, and Erta 'Ale. We find that in northern and central Afar, the majority of extension is accommodated close to the rift axis (±15–30 km). In southern Afar, near the Nubia-Arabia-Somalia triple junction, amagmatic extension is distributed over 80–160 km, which may indicate an increase in rift focusing with rift maturity. We also observe rapid surface uplift and rift-perpendicular extension at the Dabbahu-Manda-Hararo rift segment with velocities of 33 ± 4 mm/yr and 37 ± 4 mm/yr respectively. These are higher than the background extension rate of 18–20 mm/yr, but have decreased by 55%–70% since 2006–2010. The data suggests that this is due to an ongoing long-lived response to the 2005–2010 rifting episode, with potential continued processes below the rift segment including a lower-crustal viscous response and magma movement. Continued observations of surface deformation provide key constraints on tectono-magmatic processes involved in rift development.

Plain Language Summary The Afar region, which includes parts of Northern Ethiopia, Djibouti and Eritrea, is located where three tectonic plates are pulling apart. This "rifting" occurs in segments, each of which is 50–100 km long. Some segments are associated with extensive volcanic activity, with intrusions of molten rock (magma) along the rift causing extension; others lack magma and extension occurs through slip on tectonic faults. Deformation is not constant in time, with "episodes" of rifting occurring periodically and magma intrusions causing sudden ground movements. We process large quantities of radar data from the European Sentinel-1 satellites to measure very precisely the ground movements that occurred during the period 2014–2019, combining the data from different satellite tracks to produce maps of the ground movement in three directions (perpendicular to the rift zone, parallel to the rift zone, and vertical). The data show that extension is tightly focused around the volcanic segments and broadly distributed around those lacking volcanism. One segment, where a major rifting episode occurred between 2005 and 2010, still shows accelerated motions; at least four volcanic centers show evidence of subsurface magma movement. Continued observation of these time-varying ground movements is important for understanding how continents breakup.

1. Introduction

It has long been hypothesized that magma plays a crucial role in the final stages of continental breakup and the early stages of sea-floor spreading (Barberi & Varet, 1977; Courtillot et al., 1999; Ebinger & Casey, 2001; White & McKenzie, 1989). The Afar rift zone, which contains triple junction between the Nubian, Somalian, and Arabian plates (Figure 1), is elevated above sea level due to the influence of the Afar plume (Furman et al., 2006; Hammond et al., 2013; Hirn et al., 1993; Schilling, 1973) and has long been a focus of studies (Barberi & Varet, 1977; Beyene & Abdelsalam, 2005; Girdler, 1970; Hayward & Ebinger, 1996; Manighetti et al., 1998; Tapponnier et al., 1990). The three arms of the Afar rift zone are segmented (Hayward & Ebinger, 1996; Manighetti et al., 1998) with extensional strain accommodated by a combination of diking and
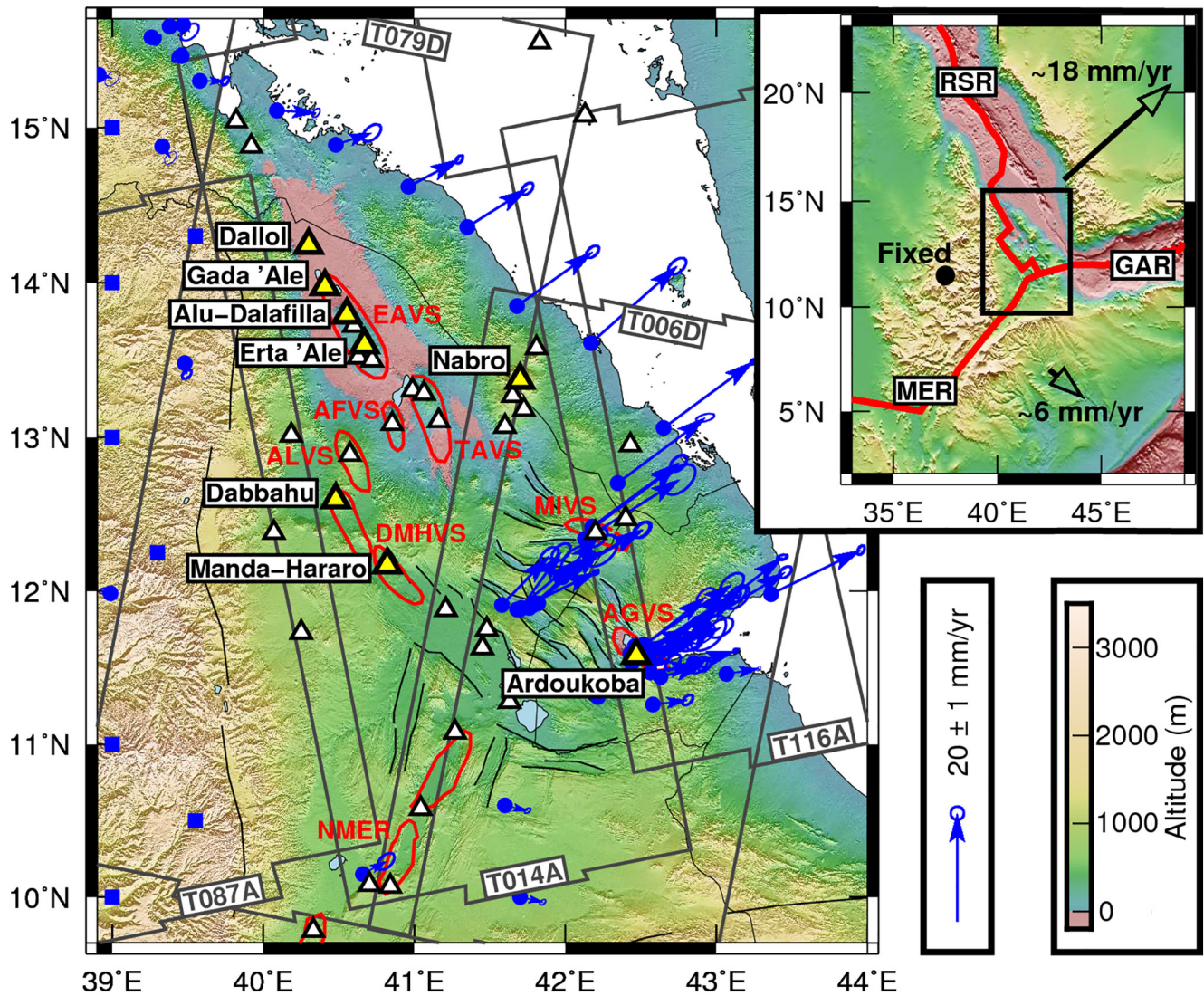
Figure 1. The Afar rift zone with white triangles indicating Holocene volcanoes and key volcanoes highlighted in yellow. Simplified volcano-tectonic segments (VS) are shown in red: AFVS, Afdera; ALVS, Alayta; AGVS, Asal-Ghoubbet; DMHVS, Dabbahu-Manda-Hararo; EAVS, Erta 'Ale; MI, Manda-Inakir; NMER, Northern Main Ethiopian Rift; TAVS, Tat 'Ale (taken from Keir et al. [2011]). Simplified faults in central Afar and simplified rift margin faults are displayed as black lines (taken from Pagli et al. [2014]). A subset of Global Navigation Satellite System (GNSS) velocity vectors with 95% confidence error ellipses (blue arrows) from King et al. (2019) show the long-term plate motions. GNSS sites from King et al. (2019) (blue circles) are supplemented by additional fabricated GNSS sites with zero velocity on the stable Nubian plate (blue squares). Gray box outlines show the Sentinel-1 coverage from three ascending (T014A, T087A, and T116A) and two descending (T006D and T079D) tracks. Inset map shows the relative movement of the Arabian and Somalian plates to the Nubian plate, with sketched plate boundaries from Bird (2003). RSR, Red Sea Rift; GAR, Gulf of Aden Rift; MER, Main Ethiopian Rift.

faulting, which varies spatially; some segments dominated by magmatism (Abdallah et al., 1979; Barberi & Varet, 1970; Wright et al., 2006) and others where amagmatic faulting is the dominant process (Sigmundsson, 1992; Tapponnier et al., 1990).

The degree of strain localization during rifting is known to be a function of lithospheric rheology, crustal thickness, heat flow, strain rate, and degree of magmatism (e.g., Buck, 1991, 2006; Corti et al., 2003; Huismans et al., 2001; Kusznir & Park, 1987). Ebinger and Casey (2001) defined three broad stages of continental breakup, which are evident in the East African Rift: (a) an early ("immature") stage where extension in the shallow lithosphere is dominated by brittle faulting on large border faults and there is only minor amounts of decompression melting, as seen for example in Tanzania (Biggs et al., 2009); (b) a "mature" stage where there is increased levels of melting, and strain localization evidenced through narrow

zones of rift-parallel diking, as seen for example at the Dabbahu-Manda-Hararo segment of the Afar rift zone (Wright et al., 2006); (c) a breakup phase where the lithosphere has thinned sufficiently such that new "oceanic" crust is effectively being formed at the ridge; they suggest the Asal rift in Djibouti (Ruegg & Pilger, 1975) is a good example of this mode. In this conceptual view, strain should become increasingly localized as magmatic continental rifting becomes increasingly "mature." However, Kogan et al. (2012) used geodetic measurements of extension across three segments of the rift system (Southern Main Ethiopian Rift, Central Main Ethiopian Rift, "Afar") to suggest that strain becomes more diffuse as magmatic continental rifting progresses.

In this paper we combine dense geodetic observations of crustal motion from Sentinel-1 interferometric synthetic aperture radar (InSAR) time series analysis with sparse point measurements from Global Navigation Satellite System (GNSS) data to produce spatially dense grids of 3D surface velocities for the entire Afar region for the period 2014–2019. We use these to map the degree of strain localization for magmatic and amagmatic rift segments and to test whether strain localizes as rifting progresses. The 2005–2010 rifting episode at the Dabbahu-Manda-Harraro segment (Grandin, Socquet, Doin, et al., 2010; Hamling et al., 2010) created a large deformation response in the lithosphere (Hamling et al., 2014; Nooner et al., 2009; Pagli et al., 2014); here we also examine how that transient feature has evolved through time. We also present the recent time history of deformation at eruptive centers in Afar.

2. Regional Setting

Upwelling of a mantle plume initiated rifting in Afar around 30 Ma with abundant flood-basalt volcanism, which has evolved into the ridge-ridge-ridge triple junction observed in Afar today (e.g., Furman et al., 2006; Hammond et al., 2013; Schilling, 1973; White & McKenzie, 1989; Wolfenden et al., 2004). Relative to the Nubian Plate, GNSS observations show that the Arabian Plate is moving at a rate of 18–20 mm/yr to the NE (ArRajehi et al., 2010; Doubre et al., 2017; McClusky et al., 2010; Viltres et al., 2020), accommodated by the opening of the Red Sea Rift; while the Somalian Plate is moving to the SE at ~6 mm/yr (Birhanu et al., 2016; Saria et al., 2014), accommodated by the Main Ethiopian Rift (MER) which is the northern-most segment of the larger East African Rift.

The crust beneath the Afar rift zone is significantly thinned in comparison to the surrounding Ethiopian Highlands and MER. Crustal thicknesses range from 20 to 45 km in the Ethiopian Plateau, 18–30 km in central Afar, and 15–20 km in northern Afar (Bastow & Keir, 2011; Hammond et al., 2011; Lavayssière et al., 2018; Tiberi et al., 2005). Low seismic velocities indicate partial melt within the crust (Gallacher et al., 2016), particularly below rift segments in Afar (Hammond, 2014; Hammond & Kendall, 2016; Stork et al., 2013). Seismicity in the upper and lower crust along the Erta 'Ale volcano-tectonic segment also indicates the presence of melt below the Erta 'Ale and Alu-Dalafilla volcanic centers (Illsley-Kemp et al., 2018).

Active volcanism in Afar is largely concentrated within discrete rifting segments (e.g., Barberi & Varet, 1978; Hayward & Ebinger, 1996; Manighetti et al., 1998). The Erta 'Ale segment in the northern-most portion of the Afar rift zone is the immediate on-land expression of the Red Sea Rift (Barberi & Varet, 1970; Barberi et al., 1970). Erta 'Ale volcano on the Erta 'Ale segment is host to a lava lake with recent overflows in 2010 (Barnie, Oppenheimer, & Pagli, 2016; Field et al., 2012) and 2017, where a flank eruption indicated the presence of a shallow magma body at ~1 km depth (Moore et al., 2019; Xu et al., 2017). At Gada 'Ale, magma withdrawal and normal faulting caused subsidence from 1993 to 1996 (Amelung et al., 2000), and a dyke intrusion fed from a magma chamber 2–3 km below Dallol was detected in 2004 (Nobile et al., 2012). The 2008 eruption at Alu-Dalafilla was sourced from a ~1 km deep axis-aligned reservoir and a magma chamber at ~4 km depth (Pagli et al., 2012).

The most significant recent volcano-tectonic rifting episode in Afar occurred from 2005 to 2010 on the Dabbahu-Manda-Hararo volcano-tectonic segment in the central portion of the Afar rift zone (e.g., Barnie, Keir, et al., 2016). The initial dyke in September 2005 ruptured the whole 60 km long rift segment, and intruded 2.4–2.6 km^3 of magma over ~2 weeks (Grandin et al., 2009; Wright et al., 2006). Seismicity was observed beneath the Dabbahu and Gabho volcanoes at the northern end of the Dabbahu-Manda-Hararo segment, before focusing on the segment center from where dykes propagated along the whole segment (Ayele et al., 2009; Grandin et al., 2011). Thirteen subsequent dykes were emplaced between 2006 and 2010,

drawing comparisons to the 1975–1984 Krafla rifting episode where extension in both settings is accommodated by magmatic intrusions (Barnie, Keir, et al., 2016; Ferguson et al., 2010; Grandin, Socquet, Jacques, et al., 2010; Hamling et al., 2010; Wright et al., 2012). Throughout the rifting episode there was an ongoing post-rifting response to the initial 2005 intrusion, which was modeled using magmatic sources in the upper crust, and the inflation of a deeper source at the segment center, as viscoelastic relaxation alone was insufficient to reproduce geodetic observations (Grandin, Socquet, Doin, et al., 2010; Hamling et al., 2014).

The Manda-Inakir and Asal-Ghoubbet volcano-tectonic segments in the southern portion of the Afar rift zone have also shown recent activity with the 1928–1929 eruption of Kammourta volcano in the Manda-Inakir volcano-tectonic segment (Audin et al., 1990), and the 1978 eruption at Ardoukoba volcano in the Asal-Ghoubbet segment (Allard et al., 1979; Tarantola et al., 1979). A post-rifting response was identified in the Asal-Ghoubbet segment to the 1978 eruption, with rift-perpendicular velocities decaying back to the long-term spreading rate 6–8 years after the eruption (Cattin et al., 2005; Ruegg & Kasser, 1987; Ruegg et al., 1993).

The Nabro Volcanic Range (NVR) is an off-axis volcanic center that sits within the Danakil Block, a rigid micro-plate which is moving away from Nubia with extension in Afar (e.g., Eagles et al., 2002; Manighetti et al., 2001; McClusky et al., 2010; Schult, 1974). The NVR has hosted explosive eruptions at Dubbi volcano in 1861 (Wiart & Oppenheimer, 2000), and Nabro volcano in 2011 (Goitom et al., 2015; J. E. Hamlyn et al., 2014). Persistent subsidence was detected at Nabro for >1 year following the 2011 eruption which was attributed to viscoelastic relaxation around a magma chamber at 6.4 ± 0.3 km depth (J. Hamlyn et al., 2018).

3. InSAR Velocity Methods and Applications in Afar

Methods for extracting a one-dimensional line-of-sight (LOS) displacement time series from a sequence or network of interferograms are well established. These small baseline algorithms utilize multiple interferogram connections between acquisition dates to produce a more robust estimate of the incremental LOS ground displacement than a simple stacking of interferograms (Berardino et al., 2002; Biggs et al., 2007; Lanari et al., 2007). This methodology may be automated by software packages such as Π-RATE (Wang et al., 2012, and references therein), StaMPS (Hooper et al., 2012), GIAnT (Agram et al., 2013), and LiCSBAS (Morishita et al., 2020) in order to obtain linear displacement rates and uncertainties at each pixel, while reducing the effect of common sources of error such as atmospheric and orbital delays. These methods may be supplemented by additional filtering to remove the atmospheric phase screen (APS) from the time series, by first high-pass filtering in time, then low-pass filtering in space to calculate the APS, which is then removed from the time series (e.g., Sousa et al., 2011). The conventional method for APS calculation relies on the assumption that the atmospheric delay is not temporally correlated. With recent SAR missions providing shorter satellite re-visit times, this assumption may no longer be appropriate. Previous studies have proposed improvements to the APS correction, including applying a global weather model (e.g., Jung et al., 2013), and accounting for the temporal variance of a pixel (e.g., Liu et al., 2011; Refice et al., 2011).

The only previous InSAR derived velocity map covering the whole Afar region was developed by Pagli et al. (2014), who used Π-RATE to produce a displacement time series between 2005 and 2010. After removing large deformation steps associated with the Dabbahu-Manda-Hararo dyke intrusion events, Pagli et al. (2014) smoothed the time series by removing the APS, employing consistent Gaussian temporal and Butterworth spatial filters. Pagli et al. (2014) extracted 3D (east, north, vertical) velocities from ascending and descending LOS and GNSS observations on a 10–20 km resolution mesh following the method of Wang and Wright (2012). Surface velocities between 2005 and 2010 from Pagli et al. (2014) showed a long-term plate spreading rate of 15–20 mm/yr in Eastern Afar (relative to a stable Nubian plate), and large extension rates of ~100 mm/yr at Dabbahu associated with the background response during the 2005–2010 Dabbahu-Manda-Hararo rifting episode. Other InSAR velocity maps within Afar have focused on individual rift segments, such as the Dabbahu-Manda-Hararo segment (Hamling et al., 2014) from 2006 to 2010, the Asal-Ghoubbet segment from 1997 to 2005 (Doubre & Peltzer, 2007) and 2003–2010 (Doubre et al., 2017), and around the Tendaho Graben from 2004 to 2010 (Temtime et al., 2018).

In this study, we make use of the high temporal and spatial resolution data from the Sentinel-1 satellite to extract surface velocities from 2014 to 2019 across the whole of the Afar region. We develop and apply a

small baseline methodology with spatial and temporal variance weighted filtering to improve the removal of the APS, reference the data to a stable Nubia GNSS reference frame, and calculate 3D (vertical, rift-perpendicular horizontal, and rift-parallel horizontal) velocities.

4. Data Processing and Time Series Methods

4.1. Sentinel-1 Data

We use Sentinel-1A/B acquisitions from ascending tracks 14 (014A), 87 (087A), and 116 (116A), and descending tracks 6 (006D) and 79 (079D) between October 2014 and August 2019. For processing efficiency, we divide each track into 12 (~250 × 250 km) frames (Table S1 in Supporting Information S1). We produce a network of geocoded unwrapped interferograms for each frame (Figure S1 in Supporting Information S1) from single-look complex (SLC) images of each date using the LiCSAR software (González et al., 2016; Lazeckỳ et al., 2020), which automates the mass production of interferograms using GAMMA (Werner et al., 2000). To reduce noise and data size, we multi-look the SLCs at 20:4 range to azimuth looks, equating to ~100 × 100 m pixel size. We apply a topographic correction using an SRTM (Shuttle Radar Topography Mission) 3-arc-second (~90 m resolution) DEM (Digital Elevation Model) (Farr & Kobrick, 2000), filter the interferograms using using a power spectrum filter (Goldstein et al., 1998), and unwrap using SNAPHU (Chen & Zebker, 2002). We manually quality check the interferogram network for each frame to remove interferograms with decorrelation, co-registration, or obvious unwrapping errors. We ensure that each epoch is connected to the network by a minimum of three interferograms by creating new interferograms as needed. Each interferogram is referenced to the mean value, excluding areas of deformation around volcanic centers.

To mitigate for atmospheric phase delay for each interferogram we compare the effectiveness of corrections from a linear trend of phase with elevation over the whole frame (e.g., Elliott et al., 2008), and the GACOS atmospheric model (e.g., Yu et al., 2017, 2018). For a linear phase-elevation trend correction, the mean root-mean-square (RMS) misfit for all 12 frames is reduced by 2.9 mm in comparison to the mean RMS misfit for all frames with no atmospheric correction. The GACOS correction gives a reduction in mean RMS misfit of 4.2 mm, but increases the RMS misfit in 29% of interferograms. To reduce this we follow an approach similar to Shen et al. (2019), scaling the GACOS correction for each interferogram in order to minimize the resulting RMS misfit. This improves the atmospheric correction further, producing a reduction in mean RMS misfit of 5.7 mm (see Figure S2 in Supporting Information S1). In order to account for any residual topographic atmospheric signal in each frame, we remove a linear trend of phase with elevation from each epoch, after time series filtering.

4.2. Time Series

We apply an SBAS style methodology to invert for the displacement time series at each pixel in the frame, using all interferograms where a pixel is coherent. We assess the spatial and temporal variance of the time series by first, filtering using a Laplacian filter with a temporal width of three epochs and scale factor of 3, then calculating the RMS misfit from this trend at each pixel for every epoch. We calculate the spatial distribution of RMS misfit from the time series misfits at each point, and the temporal distribution of RMS misfit from the misfits of all pixels at each epoch (see Figure S3 in Supporting Information S1). To resolve the RMS misfit value of each pixel at every epoch, we scale the spatial RMS misfit map to the temporal RMS misfit value at each epoch (see Supporting Information S1). We use these error estimates to provide weights during time series filtering, and in the inversion of filtered displacement time series for average velocities.

In order to reduce the remaining APS in the displacement time series, we filter the time series using a high-pass temporal and a low-pass spatial filter to produce the APS, which we then remove from the time series. To calculate a low-pass temporal filter, we apply a weighted linear trend with a fixed temporal width of 1 year centered on each point. To calculate the weighting for the local trend, we use the RMS misfit as a proxy for standard error, and convert the RMS misfit values into weights using the Bi-Square function where no weight is given to RMS values that exceed 6 standard deviations of the local misfits (e.g., Cleveland & Devlin, 1988). We also scale these weights by their temporal distance from the target epoch of the local time series (see Supporting Information S1). Having calculated the low-pass temporal filter, we remove it from

the time series to create a high-pass temporal filter. We then apply a Gaussian spatial filter with a half-width of ~2 km in order to resolve the APS for each epoch.

After we remove the APS, we remove a planar ramp in space and a linear trend with height to correct for any remnant long-wavelength and elevation-correlated atmospheric delay. We later restore any long-wavelength deformation removed here, using GNSS observations, which we assume correctly capture deformation on length scales of the ~250 × 250 km Sentinel-1 frames. For each frame, we compute the average velocity at each pixel by inverting for a single linear trend through time, allowing for a constant offset. We produce a variance-covariance matrix (VCM) for each pixel, treating the temporal variation of the scaled RMS misfit as independent errors. By including the VCM in the inversion, we can quantify the uncertainty of the resulting velocities.

De Zan et al. (2015) demonstrate how a potential systematic phase-bias in interferograms with decreasing temporal baseline can influence the resulting time series. We test the magnitude of this bias by selecting consecutive 12, 24, and 36-day interferograms from frame 079D_07694_131313 covering ~1 year (see Figure S4 in Supporting Information S1). We use a "daisy-chain" stack approach to resolve the cumulative displacements from the 12, 24, and 36 days unwrapped interferograms between December 2017 and February 2019. Any differences between these stacks indicates the presence of phase-bias and/or unwrapping errors. We find residual differences between the 12 and 24-day, and 12 and 36-day stacks of up to 50 mm, and residuals of up to 10 mm between the 24 and 36-day stacks. While this indicates that the 12-day interferograms are susceptible to a phase-bias, we find that removing the 12-day interferograms from the network effects our displacement time series by <5 mm per epoch, and our average velocities by <1 mm/yr. While we are not able to account for any bias in the 36-day interferograms, Ansari et al. (2020) indicate that the velocity bias is small in comparison to 12-day interferograms.

4.3. 3D Velocities

We tie frames together within their respective tracks by sub-sampling the InSAR data points to a 5 × 5 km spacing in the overlap between frames, and 10 × 10 km spacing elsewhere, then solving for and removing a planar ramp for each frame that minimizes residuals in the along-track frame overlap regions. Removing these ramps does not bias the results as long-wavelength signals are later corrected using GNSS data. In the frame overlap region, we use the mean value of LOS velocity for each point. We find that using linear ramps to combine frames within tracks produces the fewest boundary artifacts when compared to using a single offset value calculated from the median value in the frame overlap region, or solving for a 2D quadratic function for each frame. Boundary artifacts within tracks can occur due to differences between frames in time series length, the variation in acquisition dates used, relative weighting during time series filtering, and orbital ramp removal. Although in principle it would be possible to only process and use interferograms that cover the whole along-track extent of the study region, this would require excluding several epochs where data were not acquired over the whole area, resulting in truncated time series.

To reference the LOS velocity in each track to a stable Nubian plate, we use a network of 105 GNSS stations in the Afar region to characterize long-wavelength plate motions. These data are a subset of the Geo-PRISMS community velocity field for East Africa in a Nubia-fixed International Terrestrial Reference Frame (ITRF2014), and include continuous and campaign observations acquired between 1994 and 2018 with time spans of ≳2.4 years (King et al., 2019). For details of the data sources included, see King et al. (2019). We assume that these velocities are steady-state and do not vary significantly through time. We remove 32 stations in central Afar where the velocities are not steady-state, but are dominated by the ground motions associated with the 2005–2010 Dabbahu-Manda-Hararo rifting episode. As the resulting network is sparse (Figure S5 in Supporting Information S1), with the majority of stations concentrated in Eastern Afar and few points on the Nubian and Somalian plates; we add 17 additional fabricated GNSS stations on the stable Nubian plate, with an assumed zero velocity (with uncertainties of ±1 mm/yr and ±2 mm/yr in the horizontal and vertical components), to help constrain the velocity field where data are sparse. We project East and North GNSS horizontal velocities into the rift-perpendicular (e.g., Hamling et al., 2014), and rift-parallel directions, oriented at 61° and −29°N respectively.

From this network, we interpolate a smooth GNSS velocity field in the rift-perpendicular and rift-parallel directions over the whole Afar region at 100×100 m grid spacing (Figure S5 in Supporting Information S1) using the natural neighbor algorithm (e.g., Boissonnat & Cazals, 2002). As the additional pseudo-observations define where this interpolated field reaches zero velocity, we selected these points such that they are on the Nubian plate, away from the rift border faults. We are not concerned with the precise locations, as where the interpolated velocity field reaches zero does not significantly influence the data within the Afar Rift. We estimate the error in the interpolated velocities by systematically removing each GNSS station from the network, interpolating new velocity fields in the rift-perpendicular and rift-parallel directions from the reduced network, then calculating the residual between the interpolated fields and the GNSS observation. We take the standard deviation of these residuals as the error in the rift-perpendicular and rift-parallel GNSS velocity field.

We sub-sample the InSAR LOS track velocities as previously, then extract points where there are ascending, descending, and interpolated GNSS data. We also mask points around the active rift segments so that volcanic ground deformation does not interfere with the referencing to the long-term plate motions. Using these points, we solve for the 3D velocity (rift-perpendicular, rift-parallel, vertical) at each point and a residual 2D (East, North) quadratic function for each track. We remove the respective quadratic from each InSAR track to resolve LOS velocity in a stable Nubia reference frame. The resulting LOS velocities and standard deviations are shown in Figure 2 and Figure S5 in Supporting Information S1 respectively.

In order to resolve a full 3D velocity field (vertical, rift-perpendicular horizontal, rift-parallel horizontal) at 100×100 m resolution, we use the smooth rift-parallel GNSS field to provide a constraint on the rift-parallel velocity at each point, as the long wavelength rift-parallel velocities are small in comparison to the rift-perpendicular and vertical velocities. We include this constraint with the ascending and descending LOS InSAR observations to calculate 3D velocities at each point using a least squares inversion (Hussain et al., 2016; Weiss et al., 2020; Wright et al., 2004). The decomposition of InSAR LOS velocities (L) into rift-perpendicular ($H1$), rift-parallel ($H2$), and vertical (Z) velocities is shown in Equation 1 for the incidence angle (θ), satellite heading (α), rift angle from North (ϕ). We weight the inversion and resolve uncertainties by including a diagonal VCM using the previously calculated variance at each point.

Results (Figure 3), discussed in Section 5, show both the long-term plate motion and surface deformation associated with magmatism and transient tectonics. As we use the interpolated GNSS velocity field as an additional constraint in the rift-parallel direction, the resulting velocity field is not sensitive to short-wavelength rift-parallel deformation, which could be locally significant (Smittarello et al., 2016). As the rift-parallel error estimates also derive from the interpolated GNSS data, they are lower than the rift-perpendicular errors, which we calculate using only the InSAR observations to retain high spatial resolution (see Figure 3).

$$L = [-\sin(\theta)\cos(\alpha + \phi) + \sin(\theta)\sin(\alpha + \phi) - \cos(\theta)] \begin{bmatrix} H1 \\ H2 \\ Z \end{bmatrix} \qquad (1)$$

5. Key Findings and Discussion

5.1. Plate Motions and Uncertainties

Our 2014–2019 horizontal velocity maps (Figure 3) show the rift-perpendicular extension over the Afar rift zone at rates of up to 25 ± 5 mm/yr, with negligible long-wavelength motions in the rift-parallel direction. We also observe the gradual North to South transfer of extension from the Red Sea Rift into the Afar rift zone between ~13–16°N, indicative of the rotation of the Danakil micro-plate relative to the stable Nubian plate (e.g., Kidane, 2016; Manighetti et al., 2001; Viltres et al., 2020).

Areas of noise up to ±10 mm/yr over the Ethiopian Highlands region on the Nubain plate, are highlighted in the standard deviation maps shown in Figure 3. The regions of high error in T087A, and the northern-most portion of T014A (see Figure S6 in Supporting Information S1), are a result of the shorter time series length in these regions producing more uncertainty in the long-term velocity estimates. Elsewhere, errors of up to ±5 mm/yr are likely due to uncorrected atmospheric delays, and artifacts over track boundaries, where we are unable to account for small LOS velocity variations between overlapping tracks. These discontinuities
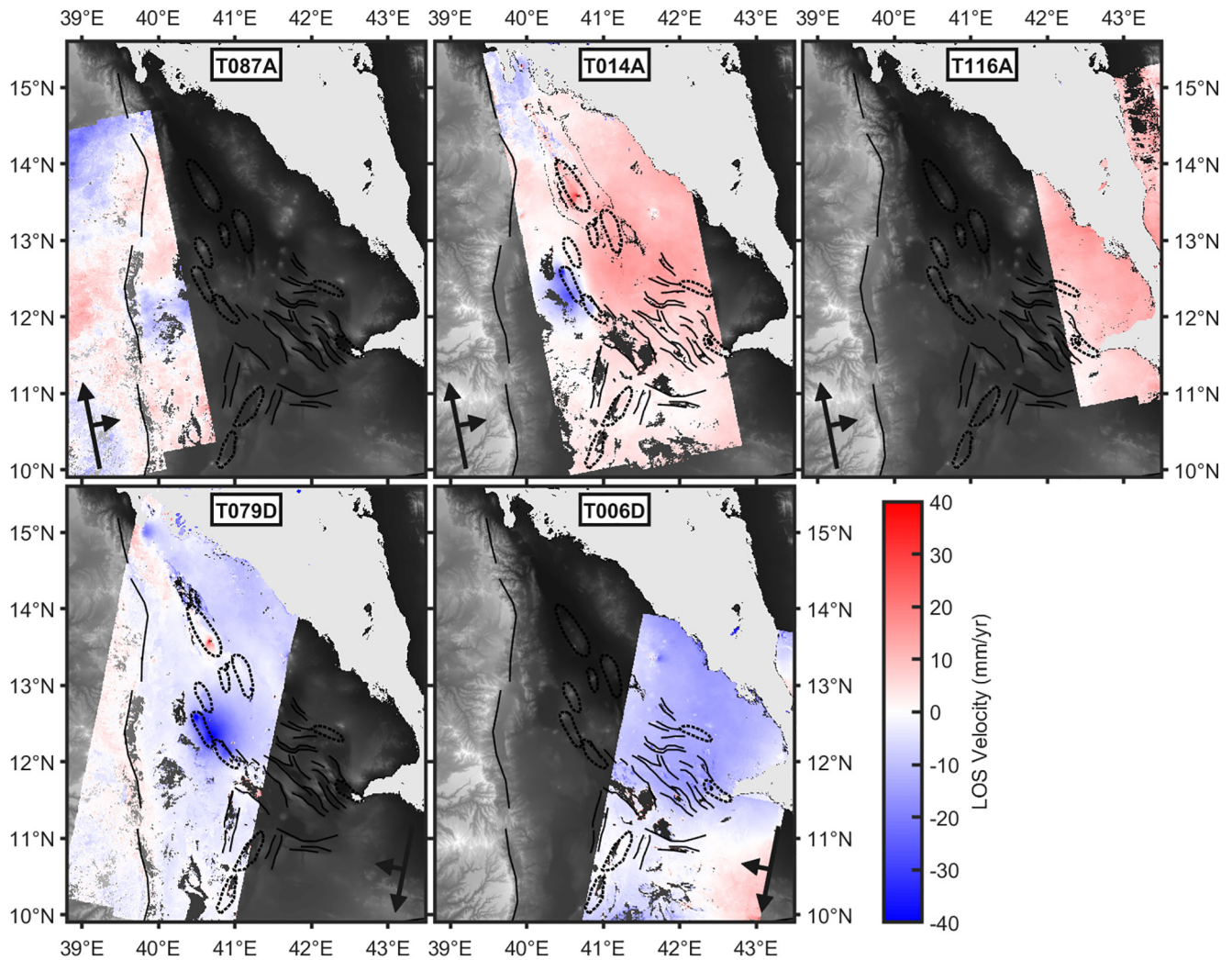
Figure 2. Line-of-sight (LOS) average velocities over the Afar region between November 2014 and August 2019 from Sentinel-1 tracks T087A, T014A, T116A, T079D, and T006D. LOS velocities are referenced to a stable Nubia reference frame using long-term plate motions from the regional Global Navigation Satellite System network (King et al., 2019). Arrows indicate the track look directions. Volcano-tectonic segments and key faults are shown as black dashed outlines and black solid lines respectively.

may arise from variations in atmospheric filtering between overlapping frames, and in GNSS referencing between overlapping tracks. The relatively uniform errors in the rift-parallel direction are due to the GNSS velocity field being used to constrain the velocities in this component, where the velocities are small in comparison to the vertical and rift-perpendicular components.

Using the overlap region between each of the tracks, we test the internal consistency of our LOS InSAR data using cross-validation by excluding each track in turn from the 3D inversion, projecting the resulting velocity field into the LOS of the excluded track, and calculating the residuals. The RMSE of the residuals in each track overlap region (Figure S7 in Supporting Information S1) range from 2.7 to 4.2 mm/yr. These are consistent with the combination of the uncertainties in our LOS velocities (1.5–6.6 mm/yr) and the propagated uncertainties of the predicted LOS velocities from our 3D velocity field with one track excluded (2.8–2.9 mm/yr), and support our estimate of uncertainties shown in Figure 3.

We also isolate the contribution of the LOS InSAR velocities to the rift-perpendicular and rift-parallel horizontal velocity maps by subtracting the interpolated GNSS velocities from the final 3D velocity map. We only test the horizontal directions of the velocity field here as we do not use GNSS data to constrain the vertical direction. As shown in Figure S8 in Supporting Information S1, velocities in the rift-perpendicular
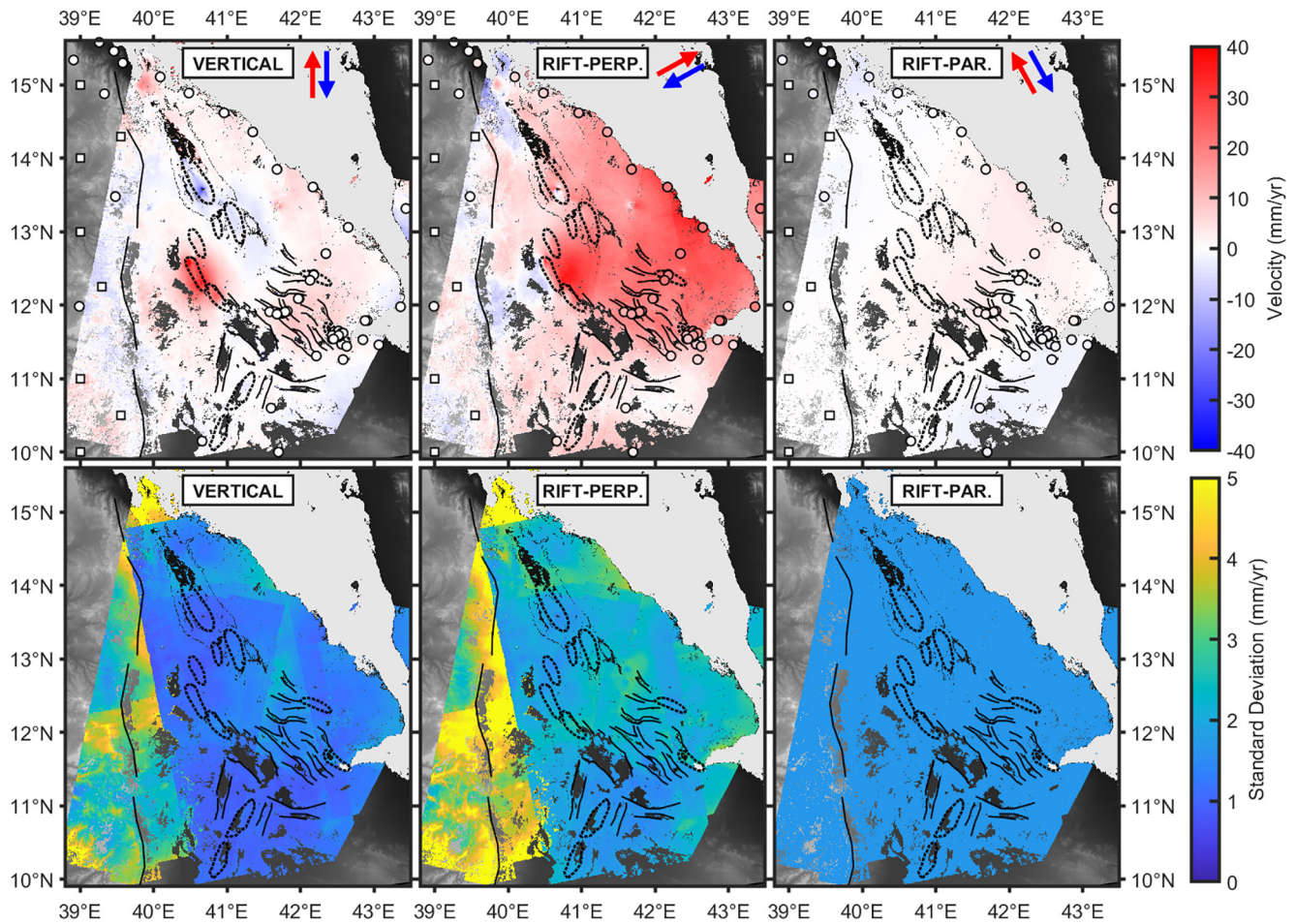
Figure 3. Vertical, rift-perpendicular, and rift-parallel average velocities and standard deviation over the Afar region between November 2014 and August 2019. All velocities are referenced to a stable Nubian plate. Vertical velocities are positive upwards, rift-perpendicular velocities are positive to the NE (61°N), and rift-parallel velocities are positive to the NW (−29°N). Standard deviation color-scale is limited to 5 mm/yr to highlight variation in regions of low variance. Maximum standard deviations are (2 s.f.): 7.2 mm/yr (vertical), 9.5 mm/yr (rift-perpendicular), and 1.7 mm/yr (rift-parallel). Real (circles) and fabricated (squares) GNSS stations used in the inversion are shown with GNSS velocities on the same color-scale as the InSAR velocities. Volcano-tectonic segments and key faults are shown as black dashed outlines and black solid lines respectively.

direction use contributions from both InSAR and GNSS, while the rift-parallel velocities are constrained only by the GNSS component as described previously. In the rift-perpendicular direction, the InSAR component is dominated by local tectono-magmatic signals and residual atmospheric and processing artifact signals, indicating that our referencing of LOS InSAR velocities to far-field plate motions is robust.

5.2. Rift Extension and Focusing

Profiles taken across the rift zone highlight the focusing of extension in Afar. Profiles covering the Alid graben, at northern-most tip of the Afar rift zone (Figures 4b and 5b), show that a broad uplift and extensional signal of up to ~20 mm/yr is centered within ±10–15 km of the rift axis. This may be indicative of deep magmatic intrusion in an area with the smallest background extension rates throughout Afar, but comparable to extension rates at the active volcanic islands at the southern end of the oceanic Red Sea Rift (Eyles et al., 2018). Uncertainty estimates in this region are also significantly higher than elsewhere in Afar and as such we do not investigate this signal any further. Profiles traversing the Erta 'Ale segment in the Danakil Depression (Figures 4c and 5c) highlight that the majority of extension here is focused into a region within ±15–20 km of the rift axis. Outside of this region, the rate of extension does not significantly vary, with velocities in agreement with long-term GNSS observations (Figure 4c). We also observe subsidence
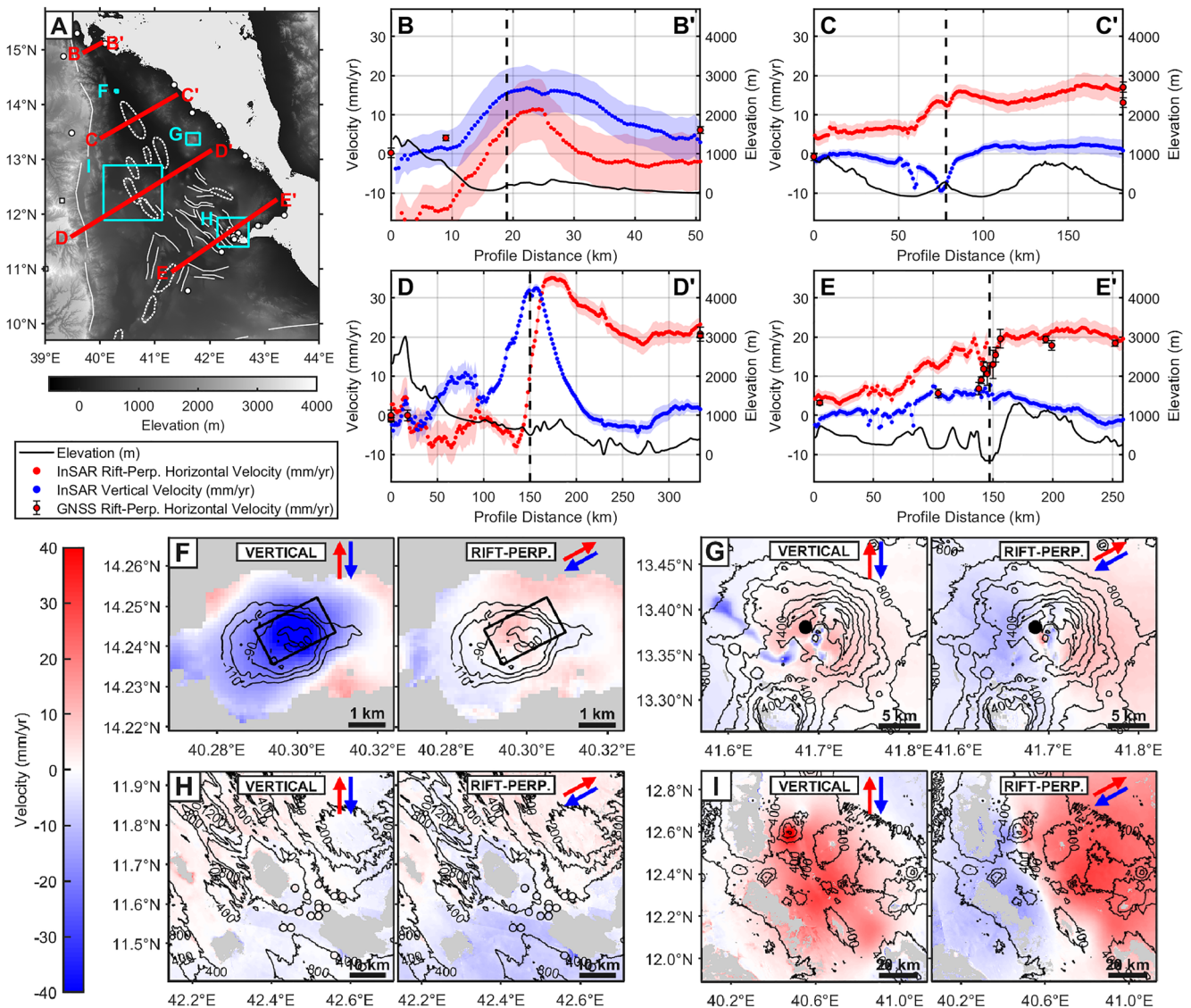
Figure 4. (a) The location of profiles (b–e) and subsets (f–i), with rift segments shown by white dashed outlines, and faults by solid white lines. The location of real (white circles) and fabricated (white squares) Global Navigation Satellite System (GNSS) sites used in (b–e) are shown in (a). Where GNSS sites are beyond the extents of the profiles, they are displayed at the profile limits on (b–e). (b–e) Vertical (blue, positive up) and rift-perpendicular (red, positive toward 61°N) velocities over 4 10 km wide cross-rift profiles marked on insert map, covering (b) the northern tip of the Afar triangle, (c) the Erta 'Ale volcano-tectonic segment, (d) the Dabbahu-Manda-Hararo volcano-tectonic segment (DMHVS), and (e) the Asal-Ghoubbet volcano-tectonic segment (AGVS). Black lines show surface elevation along the profiles, with vertical dashed lines indicating the location of the major rift axis on the profile. (f–i) Vertical and rift-perpendicular velocity maps at (f) Dallol volcano, (g) Nabro volcano, (h) the AGVS, and (i) the DMHVS. Velocities in each subset are referenced to the local background mean value, with contours indicating elevation, colored circles indicating GNSS velocities, and black crosses indicating the position of deformation time series shown in Figure 6. The location of modeled deformation sources for a 0.9–1.3 km deep sill (Okada, 1985) at Dallol (F, Figure S10 in Supporting Information S1) and a 5.5–6.8 km deep point source (Mogi, 1958) at Nabro (G, Figure S11 in Supporting Information S1) are shown as black outlines.

on the Erta 'Ale segment between the Erta 'Ale and Alu-Dalafilla volcanoes (Figure 4c), which could be linked to magma withdrawal associated with the 2017–2019 eruption at Erta 'Ale (Moore et al., 2019; Xu et al., 2017, 2020).

Profiles between the Erta 'Ale volcano-tectonic segment and the Dabbahu-Manda-Hararo volcano-tectonic segment (Figure 5c) show that extension in this region is shared between the Alayta volcano-tectonic segment and the Tat 'Ale volcano-tectonic segment, and focused to within ±10–20 km of the rift segments. Profiles covering the Dabbahu-Manda-Hararo volcano-tectonic segment (Figures 4d and 5d) also show that the long-term extension is concentrated near the rift axis, with only small variations in rift-perpendicular
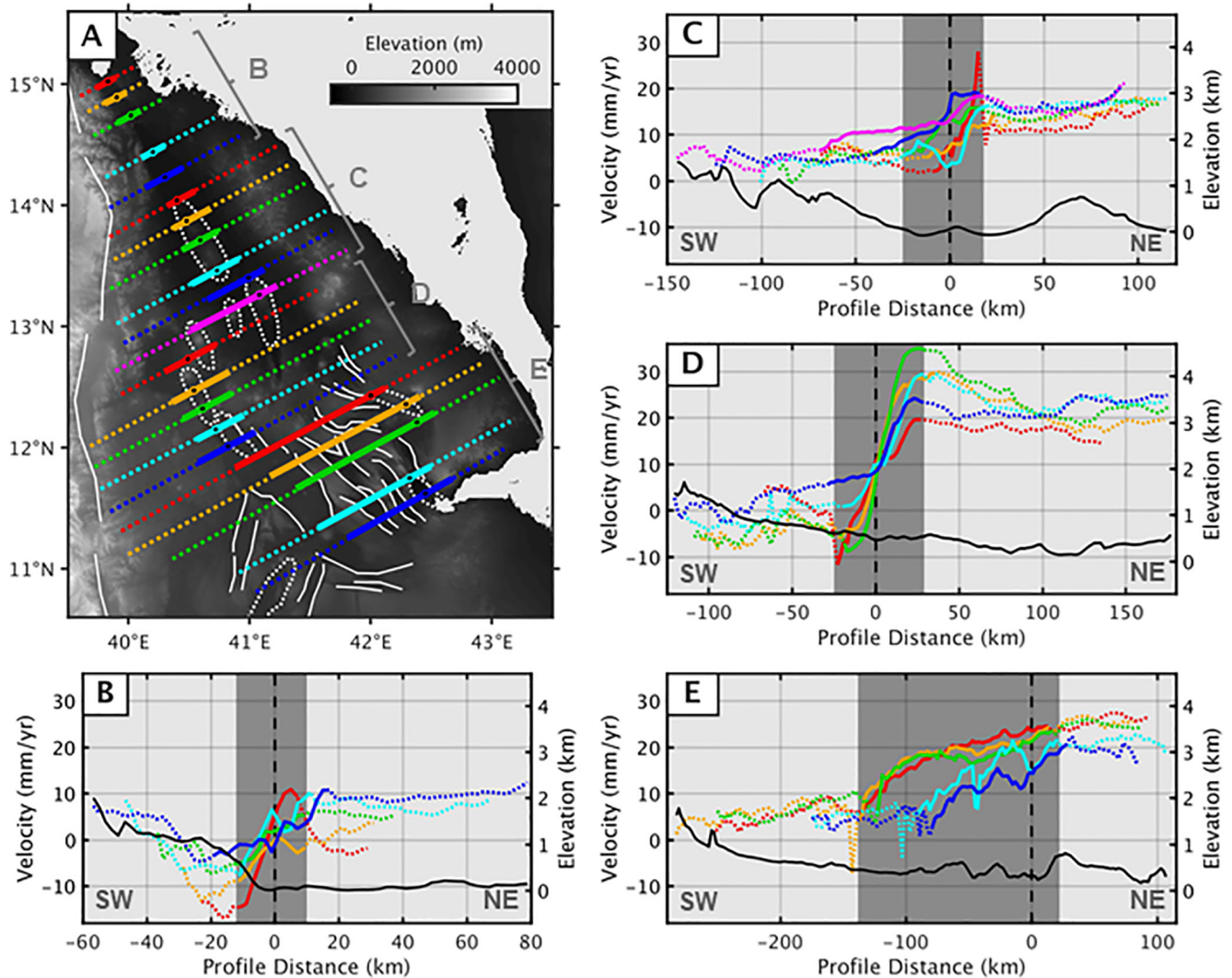
Figure 5. Map of 21 10 km wide rift-perpendicular velocity (relative to stable Nubia, positive toward 61°N) profiles over the Afar rift zone (a), with simplified rift segments shown by white dashed outlines, and simplified faults by solid white lines. The velocity profiles cover northern Afar (b), the Erta 'Ale and Tat 'Ale segments (c), the Dabbahu-Manda-Hararo segment (d), and the Manda-Inakir and Asal-Ghoubbet segments (e). The region on each profile where the majority of extension is accommodated, is indicated by the solid portion of the profile lines in (a) and (b–e), with the rest of the profile marked as dotted lines. This region of extension is approximated for each subset by the dark gray shaded portions of (b–e). The standard deviation of rift-perpendicular velocities varies from ±2–7 mm/yr (see Figure 3). The mean elevation profile for each group of profiles is shown as a solid black line. Profile distances are measured arbitrarily, relative to where the profile coincides with a magmatic segment, with positive toward the NE. Zero profile distance is marked by black circles on (a), and dashed black lines on (b–e). These profiles are shown individually with error estimates in Figure S9 in Supporting Information S1.

velocity away from ±20–30 km of the segment center. The spatial distribution of rift-perpendicular extension at the Dabbahu-Manda-Hararo segment is in agreement with the 2006–2010 InSAR derived velocities from Pagli et al. (2014), although the magnitude of extension close to the segment is reduced by 55%–70% between 2006–2010 and 2014–2019. Elevated velocities close to the segment center are associated with the 2005–2010 Dabbahu-Manda-Hararo segment rifting episode, and are discussed in Section 5.3.

Profiles over southern central Afar and the Asal-Ghoubbet segment (Figures 4e and 5e) show a more distributed pattern of extension with an initial increase in rift-perpendicular velocities 70–140 km to the SW of the rift axis near the Tendaho Graben, before velocities stabilize at ~20 mm/yr on the Danakil micro-plate within 10–20 km to the NE of the rift axis. The distribution of strain shows good agreement with GNSS observations in Figure 4e, with the differences likely occurring due to the distances between the profiles and GNSS sites (see Figure 4a) particularly for the Asal-Ghoubbet segment, where our rift-perpendicular

velocities vary strongly along the rift. In southern Afar, extension between 2014 and 2019 may be largely accommodated by tectonic rather than magmatic mechanisms, with strain being distributed across a sequence of horst and graben structures (e.g., Manighetti et al., 2001; Tapponnier et al., 1990). Previous studies have also shown that strain in southern central Afar is distributed across a broad region of the rift, with InSAR derived velocities from 2003–2010 (Doubre et al., 2017) and 2006–2010 (Pagli et al., 2014) indicating that along-profile extension is distributed over ~50–100 km and ~70–120 km respectively. The detailed GNSS observations of Doubre et al. (2017) demonstrate how this extension is accommodated within the central Afar fault structures, where extension is accommodated by tectonic processes (Manighetti et al., 1998, 2001). Pagli et al. (2019) suggest that the elevated strain and seismicity in central Afar demonstrates strain transfer between the Dabbahu-Manda-Hararo segment and Asal-Ghoubbet segment. Doubre and Peltzer (2007) and Doubre et al. (2017) also show small steps in extension close to the Asal-Ghoubbet segment with an increase of ~2–6 mm/yr over the rift segment, in agreement to the step shown in Figure 4e of ~1–7 mm/yr.

Our results indicate that at segments with current active magmatism in central and northern Afar (Erta 'Ale and Dabbahu-Manda-Hararo rift segments), extension is largely focused to within ±15–30 km of the rift axis; while in southern Afar, between the Tendaho Graben and the Manda-Inakir and Asal-Ghoubbet rift segments, extension may be distributed over 80–160 km. The broad distribution of strain in southern Afar is comparable with previous GNSS and InSAR based studies including Kogan et al. (2012), Pagli et al. (2014), and Doubre et al. (2017). Kogan et al. (2012) show that extension in southern Afar occurs over ~175 km, but also suggest that extension becomes more distributed with rift development, although their results are based on one profile through the amagmatic portion of the Afar rift zone and may also be influenced by the proximity to the triple junction. In contrast, our results suggest a possible increase in strain focusing with rift maturity during late-stage continental breakup, in keeping with strain localization assisting the transition into oceanic spreading centers (e.g., Manighetti et al., 1998), and with recent findings in the MER which suggest a northwards increase in the extension rate (Temtime, 2021). Our findings are also in keeping with other studies of rift development in Afar (e.g., Bastow et al., 2018; Keir et al., 2013), which also suggest an increase in localization in northern Afar, with significant plate thinning and extrusive magmatism.

5.3. Magmatic Deformation

Figure 4 highlights the surface deformation at Dallol (4F) and Nabro (4G) volcanoes, and at the Dabbahu-Manda-Hararo segment (4I), where localized deformation, likely associated with magma migration, is visible. As magmatic deformation may not be steady in time, we look at time series for points located in the middle of these centers. Time series of vertical displacements at the Dallol, Nabro, Dabbahu, and Manda-Hararo volcanic centers show that the deformation is reasonably linear from 2014 to 2019, indicating that the velocities displayed in Figures 4f–4i are approximately representative of 2014–2019 ground motions. For Erta 'Ale volcano, we select a point ~2 km to the north of the summit caldera in order to avoid the step surface deformation associated with a dyke intrusion in January 2017 (Moore et al., 2019; Xu et al., 2017, 2020). Following this intrusion the Erta 'Ale edifice shows linear subsidence at a rate of 15 ± 4 mm/yr (Figure 6).

Figure 4h over the Asal-Ghoubbet segment indicates the lack of significant magma related deformation at this segment from 2014 to 2019, with the change in rift-perpendicular extension over the segment being discussed in Section 5.2. Smittarello et al. (2016) observe vertical, rift-perpendicular, and rift-parallel deformation associated with post-rifting relaxation from the 1978 rifting event on the Asal-Ghoubbet segment up to 1999–2003, with a return to long-term spreading rates up to 2014 supported by Doubre et al. (2017). Our results suggest a continuation of the inter-dyking period at the Asal-Ghoubbet segment (e.g., Cattin et al., 2005; Doubre et al., 2007), with negligible vertical deformation, although we are unable to resolve any local rift-parallel deformation.

At Dallol volcano, at the northern end on the Erta 'Ale segment, we observe a high rate of subsidence of up to 45 ± 4 mm/yr, with negligible horizontal movement. The subsidence signal is focused on the central cone at Dallol. We model this signal using the Markov-Chain Monte-Carlo Geodetic Bayesian Inversion Software (GBIS) (Bagnardi & Hooper, 2018). For the T014A and T079D LOS deformation between 2014 and 2019, we test source geometries including a point pressure source (Mogi, 1958), a planar dislocation (Okada, 1985), and a penny-shaped crack (Fialko et al., 2001). We find that a ~1×2 km horizontal sill at 0.9–1.3 km depth with ~0.27 m of contraction gives the lowest residual RMS misfit (Figure S10 in Supporting Information S1).
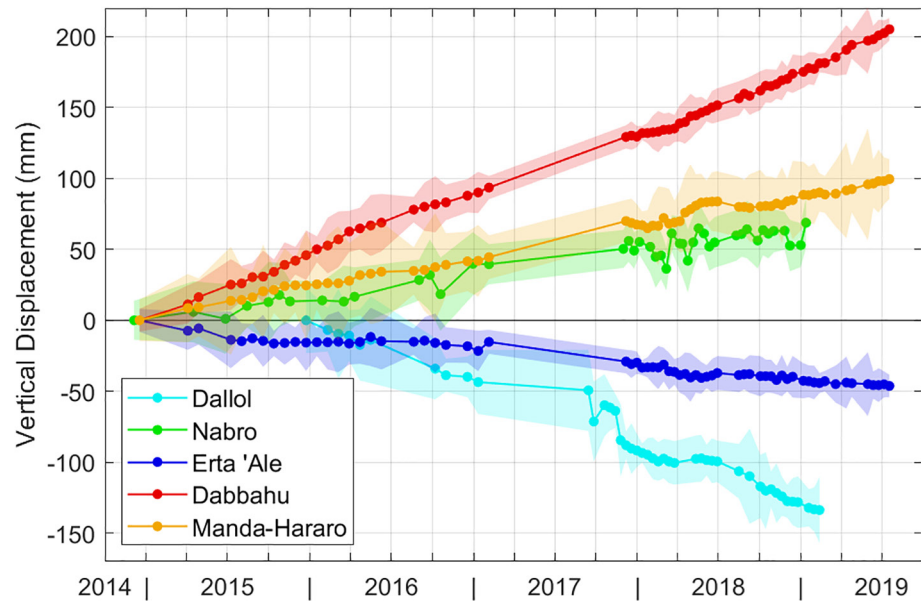
Figure 6. 2014–2019 time series of vertical displacements (uplift positive) with 1 standard deviation estimates, at 5 deforming volcanic centers in Afar. The points used for the time series are representative of the whole edifice deformation and are positioned at the center of the volcanic edifice; with the exception of Erta 'Ale where the point selected is ~2 km North of the summit lava lake in order to avoid surface deformation associated with the January 2017 dyke intrusion event (Moore et al., 2019; Xu et al., 2017, 2020). Coordinates of points used for each volcanic center: Dallol—40.3°E/14.243°N, Nabro—41.685°E/13.38°N, Erta 'Ale—40.65°E/13.62°N, Dabbahu—40.48°E/12.58°N, and Manda-Hararo—40.88°E/12.13°N.

This is in agreement with Nobile et al. (2012) who inferred the presence of a deflating magma body at 1.5–3.3 km depth beneath Dallol between 2004 and 2006, Battaglia et al. (2021) who identify a source of subsidence at 0.5–1.5 km depth, and (López-García et al., 2020) who attribute the presence of the shallow magma body to the abundant hydrothermal activity at Dallol.

At Nabro volcano, we observe edifice uplift and extension at rates of up to 12 ± 3 mm/yr, combined with the subsidence of lava flows from the 2011 eruption (J. E. Hamlyn et al., 2014), and a highly localized subsidence and contraction signal of up to 14 ± 3 mm/yr at the center of the Nabro caldera. This uplift of the Nabro edifice shows a change from InSAR observed subsidence of 150–200 mm/yr from 2011 to 2012, after the 2011 eruption (J. Hamlyn et al., 2018). As our vertical displacement time series (Figure 6) indicates that the uplift at Nabro is linear between 2014 and 2019, we suggest that this post-eruption edifice subsidence must have stopped between 2012 and 2014. We model T006D, T014A, and T079D LOS observations at Nabro volcano between 2014 and 2019 using a point pressure source (Mogi, 1958), and penny-shaped crack (Fialko et al., 2001) using GBIS (Bagnardi & Hooper, 2018). Figure S11 in Supporting Information S1 shows the optimal Mogi source at 5.5–6.8 km depth with a volume increase of $7-11 \times 10^6$ m^3. The location of this source is in agreement with the magma chamber at 6.4 ± 0.3 km depth inferred by (J. Hamlyn et al., 2018) between 2011 and 2012, suggesting re-charge of the melt storage below Nabro volcano.

After the initial 2005 intrusion at the Dabbahu-Manda-Hararo segment, background uplift and rift-perpendicular extension continued throughout the 2005–2010 rifting episode at rates of up to 80–240 mm/yr and 110–180 mm/yr respectively, from 2006 to 2010 at the segment center (Hamling et al., 2014; Pagli et al., 2014). We show that this uplift and extension is ongoing between 2014 and 2019 at average rates of 33 ± 4 mm/yr and 37 ± 4 mm/yr respectively (Figures 4c and 4h). Our vertical velocities also show that an area of ~20 mm/yr subsidence from 2006 to 2010 at the southern end of the Dabbahu-Manda-Hararo segment (40.9°E/12.1°N) uplifts at an average rate of 18 ± 4 mm/yr from 2014 to 2019. This decaying post-rifting response to the initial 2005 intrusion may be indicative of continued magma movement beneath the Dabbahu-Manda-Hararo segment and/or a time-dependant viscous response due to a more ductile rheology generated from repeated intrusions at the rift segment. Expanding on the study of Hamling et al. (2014), further

work is required to model the long-term response to the 2005–2010 rifting episode at the Dabbahu-Manda-Hararo segment, incorporating a viscous response and continued magma movement by combining the InSAR time series of Pagli et al. (2014), with the data presented here.

6. Conclusions

We develop Sentinel-1 displacement time series at 100×100 m resolution between 2014 and 2019 over three ascending and two descending tracks, covering the whole Afar rift zone. We implement a RMS misfit weighted APS correction to clean the time series, and produce average velocity maps for each frame. Using GNSS observations of long-term plate motions (King et al., 2019), we reference the InSAR velocities to the stable Nubian plate, and convert LOS into 3D velocities (vertical, rift-perpendicular, rift-parallel).

We are able to resolve deformation at individual volcanic centers, with subsidence of 45 ± 4 mm/yr at Dallol volcano, consistent with the deflation of a shallow sill at 0.9–1.3 km depth. We also show that edifice uplift at Nabro volcano of 12 ± 3 mm/yr is sourced from a magma chamber at 5.5–6.8 km depth, consistent with the source of post-eruption subsidence observed between 2011 and 2012 (J. Hamlyn et al., 2018).

Pagli et al. (2014) and Hamling et al. (2014) identify vertical and rift-perpendicular horizontal surface velocities between 2006 and 2010 of 80–240 mm/yr and 110–180 mm/yr, respectively associated with a background post-rift response to the initial 2005 dyking episode at the Dabbahu-Manda-Hararo segment. We show that this response is ongoing between 2014 and 2019, but at lower rates of 33 ± 4 mm/yr and 37 ± 4 mm/yr for uplift and rift-perpendicular extension respectively. We suggest that this ~15 years response to the 2005 dyke intrusion is indicative of continued magma movement and/or time-dependant viscous processes within the crust below the rift segment.

We resolve the long-wavelength extension over the Afar rift zone with rift-perpendicular velocities of up to 25 ± 5 mm/yr, with negligible motions in the rift-parallel direction. From cross-rift profiles, we find that extension is largely focused to within ±15–30 km of the rift axis on the active magmatic rift segments in northern Afar, while strain in central and southern Afar is distributed across 80–160 km of the rift. This trend of increased focusing of extension into northern Afar is consistent with strain localization assisting the transition into oceanic spreading centers.

Data Availability Statement

All Sentinel-1 data is sourced from the European Union Copernicus Programme. We perform data processing on the JASMIN facility, operated by the Centre for Environmental Data Analysis (CEDA), and post-processing and figure generation using MATLAB and GMT. Processed LiCSAR interferograms are available in the Centre for Environmental Data Analysis (CEDA) archive here: http://data.ceda.ac.uk/neodc/comet/data/licsar_products. Final rift-perpendicular, rift-parallel, and vertical surface velocity and estimated variance maps are also available in the CEDA archive here: http://dx.doi.org/10.5285/ac43cee2bf5e4942970492209ba95e49

References

Abdallah, A., Courtillot, V., Kasser, M., Le Dain, A. Y., Lépine, J. C., Robineau, B., et al. (1979). Relevance of Afar seismicity and volcanism to the mechanics of accreting plate boundaries. *Nature*, *282*, 17–23. https://doi.org/10.1038/282017a0

Agram, P., Jolivet, R., Riel, B., Lin, Y., Simons, M., Hetland, E., et al. (2013). New radar interferometric time series analysis toolbox released. *Eos, Transactions American Geophysical Union*, *94*(7), 69–70. https://doi.org/10.1002/2013eo070001

Allard, P., Tazieff, H., & Dajlevic, D. (1979). Observations of seafloor spreading in Afar during the November 1978 fissure eruption. *Nature*, *279*(5708), 30–33. https://doi.org/10.1038/279030a0

Amelung, F., Oppenheimer, C., Segall, P., & Zebker, H. (2000). Ground deformation near Gada 'Ale volcano, Afar, observed by radar interferometry. *Geophysical Research Letters*, *27*(19), 3093–3096. https://doi.org/10.1029/2000GL008497

Ansari, H., De Zan, F., & Parizzi, A. (2020). Study of systematic bias in measuring surface deformation with SAR interferometry. *IEEE Transactions on Geoscience and Remote Sensing*, *59*(2), 1285–1301. https://doi.org/10.1109/TGRS.2020.3003421

ArRajehi, A., McClusky, S., Reilinger, R., Daoud, M., Alchalbi, A., Ergintav, S., et al. (2010). Geodetic constraints on present-day motion of the Arabian Plate: Implications for Red Sea and Gulf of Aden rifting. *Tectonics*, *29*(3). https://doi.org/10.1029/2009TC002482

Audin, J., Vellutini, P. J., Coulon, C., Piguet, P., & Vincent, J. (1990). The 1928–1929 eruption of Kammourta volcano – Evidence of tectono-magmatic activity in the Manda-Inakir rift and comparison with the Asal Rift, Afar depression, Republic of Djibouti. *Bulletin of Volcanology*, *52*, 551–561. https://doi.org/10.1007/bf00301536

Ayele, A., Keir, D., Ebinger, C., Wright, T. J., Stuart, G. W., Buck, W. R., et al. (2009). September 2005 mega-dike emplacement in the Man-da-Harraro nascent oceanic rift (Afar depression). *Geophysical Research Letters*, *36*(20). https://doi.org/10.1029/2009GL039605

Bagnardi, M., & Hooper, A. (2018). Inversion of surface deformation data for rapid estimates of source parameters and uncertainties: A Bayesian approach. *Geochemistry, Geophysics, Geosystems*, *19*(7), 2194–2211. https://doi.org/10.1029/2018GC007585

Barberi, F., Borsi, S., Ferrara, G., Marinelli, G., Varet, J., & Marinelli, G. (1970). Relations between tectonics and magmatology in the northern Danakil Depression (Ethiopia). *Philosophical Transactions of the Royal Society of London. Series A, Mathematical and Physical Sciences*, *267*(267), 293–311. https://doi.org/10.1098/rsta.1970.0037

Barberi, F., & Varet, J. (1970). The Erta Ale volcanic range (Danakil Depression, northern Afar, Ethiopia). *Bulletin Volcanologique*, *34*(4), 848–917. https://doi.org/10.1007/BF02596805

Barberi, F., & Varet, J. (1977). Volcanism of Afar: Small-scale plate tectonics implications. *Geological Society of America Bulletin*, *88*(9), 1251–1266. https://doi.org/10.1130/0016-7606(1977)88<1251:voaspt>2.0.co;2

Barberi, F., & Varet, J. (1978). The Afar rift junction. In *Petrology and geochemistry of continental rifts* (pp. 55–69). Springer. https://doi.org/10.1007/978-94-009-9803-2_6

Barnie, T. D., Keir, D., Hamling, I., Hofmann, B., Belachew, M., Carn, S., et al. (2016). A multidisciplinary study of the final episode of the Manda Hararo dyke sequence, Ethiopia, and implications for trends in volcanism during the rifting cycle. *Geological Society, London, Special Publications*, *420*, 149–163. https://doi.org/10.1144/SP420.6

Barnie, T. D., Oppenheimer, C., & Pagli, C. (2016). Does the lava lake of Erta 'Ale volcano respond to regional magmatic and tectonic events? An investigation using Earth Observation data. *Geological Society, London, Special Publications*, *420*, 181–208. https://doi.org/10.1144/SP420.15

Bastow, I. D., Booth, A. D., Corti, G., Keir, D., Magee, C., Jackson, C. A.-L., et al. (2018). The development of late-stage continental breakup: Seismic reflection and borehole evidence from the Danakil Depression, Ethiopia. *Tectonics*, *37*(9), 2848–2862. https://doi.org/10.1029/2017tc004798

Bastow, I. D., & Keir, D. (2011). The protracted development of the continent-ocean transition in Afar. *Nature Geoscience*, *4*(4), 248–250. https://doi.org/10.1038/ngeo1095

Battaglia, M., Pagli, C., & Meuti, S. (2021). The 2008–2010 Subsidence of Dallol Volcano on the Spreading Erta Ale Ridge: InSAR Observations and Source Models. *Remote Sensing*, *13*(10), 1991. https://doi.org/10.3390/rs13101991

Berardino, P., Fornaro, G., Lanari, R., & Sansosti, E. (2002). A new algorithm for surface deformation monitoring based on small baseline differential SAR interferograms. *IEEE Transactions on Geoscience and Remote Sensing*, *40*(11), 2375–2383. https://doi.org/10.1109/TGRS.2002.803792

Beyene, A., & Abdelsalam, M. G. (2005). Tectonics of the Afar Depression: A review and synthesis. *Journal of African Earth Sciences*, *41*(1–2), 41–59. https://doi.org/10.1016/j.jafrearsci.2005.03.003

Biggs, J., Amelung, F., Gourmelen, N., Dixon, T. H., & Kim, S. W. (2009). InSAR observations of 2007 Tanzania rifting episode reveal mixed fault and dyke extension in an immature continental rift. *Geophysical Journal International*, *179*, 549–558. https://doi.org/10.1111/j.1365-246X.2009.04262.x

Biggs, J., Wright, T., Lu, Z., & Parsons, B. (2007). Multi-interferogram method for measuring interseismic deformation: Denali Fault, Alaska. *Geophysical Journal International*, *170*(3), 1165–1179. https://doi.org/10.1111/j.1365-246X.2007.03415.x

Bird, P. (2003). An updated digital model of plate boundaries. *Geochemistry, Geophysics, Geosystems*, *4*(3). https://doi.org/10.1029/2001GC000252

Birhanu, Y., Bendick, R., Fisseha, S., Lewi, E., Floyd, M., King, R., & Reilinger, R. (2016). GPS constraints on broad scale extension in the Ethiopian Highlands and Main Ethiopian Rift. *Geophysical Research Letters*, *43*(13), 6844–6851. https://doi.org/10.1002/2016gl069890

Boissonnat, J.-D., & Cazals, F. (2002). Smooth surface reconstruction via natural neighbour interpolation of distance functions. *Computational Geometry*, *22*(1–3), 185–203. https://doi.org/10.1016/s0925-7721(01)00048-7

Buck, W. R. (1991). Modes of continental lithospheric extension. *Journal of Geophysical Research: Solid Earth*, *96*(B12), 20161–20178. https://doi.org/10.1029/91jb01485

Buck, W. R. (2006). The role of magma in the development of the Afro-Arabian Rift System. *Geological Society, London, Special Publications*, *259*, 43–54. https://doi.org/10.1144/GSL.SP.2006.259.01.05

Cattin, R., Doubre, C., de Chabalier, J. B., King, G., Vigny, C., Avouac, J. P., & Ruegg, J. C. (2005). Numerical modelling of quaternary deformation and post-rifting displacement in the Asal-Ghoubbet rift (Djibouti, Africa). *Earth and Planetary Science Letters*, *239*(3–4), 352–367. https://doi.org/10.1016/j.epsl.2005.07.028

Chen, C. W., & Zebker, H. A. (2002). Phase unwrapping for large SAR interferograms: Statistical segmentation and generalized network models. *IEEE Transactions on Geoscience and Remote Sensing*, *40*(8), 1709–1719. https://doi.org/10.1109/tgrs.2002.802453

Cleveland, W. S., & Devlin, S. J. (1988). Locally weighted regression: An approach to regression analysis by local fitting. *Journal of the American Statistical Association*, *83*(403), 596–610. https://doi.org/10.1080/01621459.1988.10478639

Corti, G., Bonini, M., Conticelli, S., Innocenti, F., Manetti, P., & Sokoutis, D. (2003). Analogue modelling of continental extension: A review focused on the relations between the patterns of deformation and the presence of magma. *Earth-Science Reviews*, *63*(3–4), 169–247. https://doi.org/10.1016/s0012-8252(03)00035-7

Courtillot, V., Jaupart, C., Manighetti, I., Tapponnier, P., & Besse, J. (1999). On causal links between flood basalts and continental breakup. *Earth and Planetary Science Letters*, *166*(3–4), 177–195. https://doi.org/10.1016/s0012-821x(98)00282-9

De Zan, F., Zonno, M., & Lopez-Dekker, P. (2015). Phase inconsistencies and multiple scattering in SAR interferometry. *IEEE Transactions on Geoscience and Remote Sensing*, *53*(12), 6608–6616. https://doi.org/10.1109/tgrs.2015.2444431

Doubre, C., Déprez, A., Masson, F., Socquet, A., Lewi, E., Grandin, R., et al. (2017). Current deformation in Central Afar and triple junction kinematics deduced from GPS and InSAR measurements. *Geophysical Journal International*, *208*, 936–953. https://doi.org/10.1093/gji/ggw434

Doubre, C., Manighetti, I., Dorbath, L., Dorbath, C., Bertil, D., & Delmond, J. (2007). Crustal structure and magmato-tectonic processes in an active rift (Asal-Ghoubbet, Afar, East Africa): 2. Insights from the 23-year recording of seismicity since the last rifting event. *Journal of Geophysical Research: Solid Earth*, *112*(B5). https://doi.org/10.1029/2006jb004333

Doubre, C., & Peltzer, G. (2007). Fluid-controlled faulting process in the Asal Rift, Djibouti, from 8 yr of radar interferometry observations. *Geology*, *35*(1), 69–72. https://doi.org/10.1130/G23022A.1

Eagles, G., Gloaguen, R., & Ebinger, C. (2002). Kinematics of the Danakil microplate. *Earth and Planetary Science Letters*, *203*(2), 607–620. https://doi.org/10.1016/S0012-821X(02)00916-0

Ebinger, C., & Casey, M. (2001). Continental breakup in magmatic provinces: An Ethiopian example. *Geology*, *29*(6), 527–530. https://doi.org/10.1130/0091-7613(2001)029<0527:cbimpa>2.0.co;2

Elliott, J. R., Biggs, J., Parsons, B., & Wright, T. J. (2008). InSAR slip rate determination on the Altyn Tagh Fault, northern Tibet, in the presence of topographically correlated atmospheric delays. *Geophysical Research Letters*, *35*(12), 1–5. https://doi.org/10.1029/2008GL033659

Eyles, J. H., Illsley-Kemp, F., Keir, D., Ruch, J., & Jónsson, S. (2018). Seismicity associated with the formation of a new island in the Southern Red Sea. *Frontiers in Earth Science*, *6*, 141. https://doi.org/10.3389/feart.2018.00141

Farr, T. G., & Kobrick, M. (2000). Shuttle Radar Topography Mission produces a wealth of data. *Eos, Transactions American Geophysical Union*, *81*(48), 583–585. https://doi.org/10.1029/EO081i048p00583

Ferguson, D. J., Barnie, T. D., Pyle, D. M., Oppenheimer, C., Yirgu, G., Lewi, E., et al. (2010). Recent rift-related volcanism in Afar, Ethiopia. *Earth and Planetary Science Letters*, *292*(3–4), 409–418. https://doi.org/10.1016/j.epsl.2010.02.010

Fialko, Y., Khazan, Y., & Simons, M. (2001). Deformation due to a pressurized horizontal circular crack in an elastic half-space, with applications to volcano geodesy. *Geophysical Journal International*, *146*(1), 181–190. https://doi.org/10.1046/j.1365-246x.2001.00452.x

Field, L., Barnie, T., Blundy, J., Brooker, R. A., Keir, D., Lewi, E., & Saunders, K. (2012). Integrated field, satellite and petrological observations of the November 2010 eruption of Erta Ale. *Bulletin of Volcanology*, *74*, 2251–2271. https://doi.org/10.1007/s00445-012-0660-7

Furman, T., Bryce, J., Rooney, T., Hanan, B., Yirgu, G., & Ayalew, D. (2006). Heads and tails: 30 million years of the Afar plume. *Geological Society, London, Special Publications*, *259*, 95–119. https://doi.org/10.1144/GSL.SP.2006.259.01.09

Gallacher, R. J., Keir, D., Harmon, N., Stuart, G., Leroy, S., Hammond, J. O., et al. (2016). The initiation of segmented buoyancy-driven melting during continental breakup. *Nature Communications*, *7*, 13110. https://doi.org/10.1038/ncomms13110

Girdler, R. (1970). The structure and evolution of the Red Sea and the nature of the Red Sea, Gulf of Aden and Ethiopian Rift Junction. *Tectonophysics*, *10*(5–6), 579–582. https://doi.org/10.1016/0040-1951(70)90047-8

Goitom, B., Oppenheimer, C., Hammond, J. O., Grandin, R., Barnie, T., Donovan, A., et al. (2015). First recorded eruption of Nabro volcano, Eritrea, 2011. *Bulletin of Volcanology*, *77*(85), 1–21. https://doi.org/10.1007/s00445-015-0966-3

Goldstein, J., Reed, I., & Scharf, L. (1998). A multistage representation of the Wiener filter based on orthogonal projections. *IEEE Transactions on Information Theory*, *44*(7), 2943–2959. https://doi.org/10.1109/18.737524

González, P. J., Walters, R. J., Hatton, E. L., Spaans, K., & Hooper, A. (2016). LiCSAR: Tools for automated generation of Sentinel-1 frame interferograms. In *AGU Fall Meeting*. American Geophysical Union.

Grandin, R., Jacques, E., Nercessian, A., Ayele, A., Doubre, C., Socquet, A., et al. (2011). Seismicity during lateral dike propagation: Insights from new data in the recent Manda Hararo-Dabbahu rifting episode (Afar, Ethiopia). *Geochemistry, Geophysics, Geosystems*, *12*(4). https://doi.org/10.1029/2010GC003434

Grandin, R., Socquet, A., Binet, R., Klinger, Y., Jacques, E., De Chabalier, J. B., et al. (2009). September 2005 Manda Hararo-Dabbahu rifting event, Afar (Ethiopia): Constraints provided by geodetic data. *Journal of Geophysical Research: Solid Earth*, *114*(B8). https://doi.org/10.1029/2008JB005843

Grandin, R., Socquet, A., Doin, M. P., Jacques, E., DeChabalier, J. B., & King, G. C. P. (2010). Transient rift opening in response to multiple dike injections in the Manda Hararo rift (Afar, Ethiopia) imaged by time-dependent elastic inversion of interferometric synthetic aperture radar data. *Journal of Geophysical Research: Solid Earth*, *115*(B9). https://doi.org/10.1029/2009JB006883

Grandin, R., Socquet, A., Jacques, E., Mazzoni, N., DeChabalier, J. B., & King, G. C. P. (2010). Sequence of rifting in Afar, Manda-Hararo rift, Ethiopia, 2005–2009: Time-space evolution and interactions between dikes from interferometric synthetic aperture radar and static stress change modeling. *Journal of Geophysical Research: Solid Earth*, *115*(B10). https://doi.org/10.1029/2009jb000815

Hamling, I. J., Wright, T. J., Calais, E., Bennati, L., & Lewi, E. (2010). Stress transfer between thirteen successive dyke intrusions in Ethiopia. *Nature Geoscience*, *3*(10), 713–717. https://doi.org/10.1038/ngeo967

Hamling, I. J., Wright, T. J., Calais, E., Lewi, E., & Fukahata, Y. (2014). InSAR observations of post-rifting deformation around the Dabbahu rift segment, Afar, Ethiopia. *Geophysical Journal International*, *197*, 33–49. https://doi.org/10.1093/gji/ggu003

Hamlyn, J., Wright, T., Walters, R., Pagli, C., Sansosti, E., Casu, F., et al. (2018). What causes subsidence following the 2011 eruption at Nabro (Eritrea)? *Progress in Earth and Planetary Science*, *5*(1), 31. https://doi.org/10.1186/s40645-018-0186-5

Hamlyn, J. E., Keir, D., Wright, T. J., Neuberg, J. W., Goitom, B., Hammond, J. O. S., et al. (2014). Seismicity and subsidence following the 2011 Nabro eruption, Eritrea: Insights into the plumbing system of an off-rift volcano. *Journal of Geophysical Research: Solid Earth*, *119*, 8267–8282. https://doi.org/10.1002/2014JB011395

Hammond, J. O. S. (2014). Constraining melt geometries beneath the Afar Depression, Ethiopia from teleseismic receiver functions: The anisotropic H-κ stacking technique. *Geochemistry, Geophysics, Geosystems*, *15*(4), 1316–1332. https://doi.org/10.1002/2013gc005186

Hammond, J. O. S., & Kendall, J. M. (2016). Constraints on melt distribution from seismology: A case study in Ethiopia. *Geological Society, London, Special Publications*, *420*, 127–147. https://doi.org/10.1144/SP420.14

Hammond, J. O. S., Kendall, J. M., Stuart, G. W., Ebinger, C. J., Bastow, I. D., Keir, D., et al. (2013). Mantle upwelling and initiation of rift segmentation beneath the Afar Depression. *Geology*, *41*(6), 635–638. https://doi.org/10.1130/G33925.1

Hammond, J. O. S., Kendall, J. M., Stuart, G. W., Keir, D., Ebinger, C., Ayele, A., & Belachew, M. (2011). The nature of the crust beneath the Afar triple junction: Evidence from receiver functions. *Geochemistry, Geophysics, Geosystems*, *12*(12). https://doi.org/10.1029/2011GC003738

Hayward, N. J., & Ebinger, C. J. (1996). Variations in the along-axis segmentation of the Afar Rift system. *Tectonics*, *15*(2), 244–257. https://doi.org/10.1029/95TC02292

Hirn, A., Lépine, J.-C., & Sapin, M. (1993). Triple junction and ridge hotspots: Earthquakes, faults, and volcanism in Afar, the Azores, and Iceland. *Journal of Geophysical Research: Solid Earth*, *98*(B7), 11995–12001. https://doi.org/10.1029/93jb00373

Hooper, A., Bekaert, D., Spaans, K., & Arıkan, M. (2012). Recent advances in SAR interferometry time series analysis for measuring crustal deformation. *Tectonophysics*, *514*, 1–13. https://doi.org/10.1016/j.tecto.2011.10.013

Huismans, R. S., Podladchikov, Y. Y., & Cloetingh, S. (2001). Transition from passive to active rifting: Relative importance of asthenospheric doming and passive extension of the lithosphere. *Journal of Geophysical Research: Solid Earth*, *106*(B6), 11271–11291. https://doi.org/10.1029/2000jb900424

Hussain, E., Hooper, A., Wright, T. J., Walters, R. J., & Bekaert, D. P. (2016). Interseismic strain accumulation across the central North Anatolian Fault from iteratively unwrapped InSAR measurements. *Journal of Geophysical Research: Solid Earth*, *121*, 9000–9019. https://doi.org/10.1002/2016JB013108

Illsley-Kemp, F., Keir, D., Bull, J. M., Gernon, T. M., Ebinger, C., Ayele, A., et al. (2018). Seismicity during continental breakup in the Red Sea Rift of Northern Afar. *Journal of Geophysical Research: Solid Earth*, *123*, 2345–2362. https://doi.org/10.1002/2017JB014902

Jung, J., Kim, D.-J., & Park, S.-E. (2013). Correction of atmospheric phase screen in time series InSAR using WRF model for monitoring volcanic activities. *IEEE Transactions on Geoscience and Remote Sensing*, *52*(5), 2678–2689.

Keir, D., Bastow, I. D., Pagli, C., & Chambers, E. L. (2013). The development of extension and magmatism in the Red Sea rift of Afar. *Tectonophysics*, *607*, 98–114. https://doi.org/10.1016/j.tecto.2012.10.015

Keir, D., Pagli, C., Bastow, I. D., & Ayele, A. (2011). The magma-assisted removal of Arabia in Afar: Evidence from dike injection in the Ethiopian rift captured using InSAR and seismicity. *Tectonics*, *30*(2). https://doi.org/10.1029/2010TC002785

Kidane, T. (2016). Strong clockwise block rotation of the Ali-Sabieh/Aïsha Block: Evidence for opening of the Afar Depression by a 'saloon-door' mechanism. *Geological Society, London, Special Publications*, *420*, 209–219. https://doi.org/10.1144/SP420.10

King, R., Floyd, M., Reilinger, R., & Bendick, R. (2019). *GPS velocity field (MIT 2019.0) for the East African Rift System generated by King et al.* Interdisciplinary Earth Data Alliance (IEDA). https://doi.org/10.1594/IEDA/324785

Kogan, L., Fisseha, S., Bendick, R., Reilinger, R., McClusky, S., King, R., & Solomon, T. (2012). Lithospheric strength and strain localization in continental extension from observations of the East African Rift. *Journal of Geophysical Research: Solid Earth*, *117*(B3). https://doi.org/10.1029/2011JB008516

Kusznir, N., & Park, R. (1987). The extensional strength of the continental lithosphere: Its dependence on geothermal gradient, and crustal composition and thickness. *Geological Society, London, Special Publications*, *28*(1), 35–52. https://doi.org/10.1144/gsl.sp.1987.028.01.04

Lanari, R., Casu, F., Manzo, M., Zeni, G., Berardino, P., Manunta, M., & Pepe, A. (2007). An overview of the Small BAseline Subset algorithm: A DInSAR technique for surface deformation analysis. *Pure and Applied Geophysics*, *164*(4), 637–661. https://doi.org/10.1007/s00024-007-0192-9

Lavayssière, A., Rychert, C., Harmon, N., Keir, D., Hammond, J. O., Kendall, J.-M., et al. (2018). Imaging lithospheric discontinuities beneath the Northern East African Rift Using S-to-P receiver functions. *Geochemistry, Geophysics, Geosystems*, *19*(10), 4048–4062. https://doi.org/10.1029/2018gc007463

Lazeckỳ, M., Spaans, K., González, P. J., Maghsoudi, Y., Morishita, Y., Albino, F., et al. (2020). LiCSAR: An automatic InSAR tool for measuring and monitoring tectonic and volcanic activity. *Remote Sensing*, *12*(15), 2430.

Liu, S., Hanssen, R., Samiei-Esfahany, S., Hooper, A., & Van Leijen, F. (2011). Separating non-linear deformation and atmospheric phase screen (APS) for InSAR time series analysis using least-squares collocation. In *Proceedings of the Advances in the Science and Applications of SAR Interferometry, ESA Fringe 2009, Workshop ESA*.

López-García, J. M., Moreira, D., Benzerara, K., Grunewald, O., & López-García, P. (2020). Origin and evolution of the halo-volcanic complex of Dallol: Proto-volcanism in Northern Afar (Ethiopia). *Frontiers in Earth Science*, *7*, 351. https://doi.org/10.3389/feart.2019.00351

Manighetti, I., Tapponnier, P., Courtillot, V., Gallet, Y., Jacques, E., & Gillot, P.-Y. (2001). Strain transfer between disconnected, propagating rifts in Afar. *Journal of Geophysical Research: Solid Earth*, *106*(B7), 13613–13665. https://doi.org/10.1029/2000jb900454

Manighetti, I., Tapponnier, P., Gillot, P., Jacques, E., Courtillot, V., Armijo, R., et al. (1998). Propagation of rifting along the Arabia-Somalia plate boundary: Into Afar. *Journal of Geophysical Research: Solid Earth*, *103*(B3), 4947–4974. https://doi.org/10.1029/97jb02758

McClusky, S., Reilinger, R., Ogubazghi, G., Amleson, A., Healeb, B., Vernant, P., et al. (2010). Kinematics of the southern Red Sea-Afar Triple Junction and implications for plate dynamics. *Geophysical Research Letters*, *37*(5). https://doi.org/10.1029/2009GL041127

Mogi, K. (1958). Relations between the eruptions of various volcanoes and the deformations of the ground surfaces around them. *Bulletin of the Earthquake Research Institute*, *36*, 99–134.

Moore, C., Wright, T., Hooper, A., & Biggs, J. (2019). The 2017 eruption of Erta 'Ale volcano, Ethiopia: Insights in the shallow axial plumbing system of an incipient mid-ocean ridge. *Geochemistry, Geophysics, Geosystems*, *20*(12). https://doi.org/10.1029/2019gc008692

Morishita, Y., Lazeckỳ, M., Wright, T. J., Weiss, J. R., Elliott, J. R., & Hooper, A. (2020). LiCSBAS: An open-source InSAR time series analysis package integrated with the LiCSAR automated Sentinel-1 InSAR processor. *Remote Sensing*, *12*(3), 424. https://doi.org/10.3390/rs12030424

Nobile, A., Pagli, C., Keir, D., Wright, T. J., Ayele, A., Ruch, J., & Acocella, V. (2012). Dike-fault interaction during the 2004 Dallol intrusion at the northern edge of the Erta Ale Ridge (Afar, Ethiopia). *Geophysical Research Letters*, *39*(19). https://doi.org/10.1029/2012GL053152

Nooner, S. L., Bennati, L., Calais, E., Buck, W. R., Hamling, I. J., Wright, T. J., & Lewi, E. (2009). Post-rifting relaxation in the Afar region, Ethiopia. *Geophysical Research Letters*, *36*(21). https://doi.org/10.1029/2009gl040502

Okada, Y. (1985). Surface deformation due to shear and tensile faults in a half-space. *Bulletin of the Seismological Society of America*, *75*(4), 1135–1154. https://doi.org/10.1785/bssa0750041135

Pagli, C., Wang, H., Wright, T. J., Calais, E., & Lewi, E. (2014). Current plate boundary deformation of the Afar rift from a 3-D velocity field inversion of InSAR and GPS. *Journal of Geophysical Research: Solid Earth*, *119*, 8562–8575. https://doi.org/10.1002/2014JB011391

Pagli, C., Wright, T. J., Ebinger, C. J., Yun, S. H., Cann, J. R., Barnie, T., & Ayele, A. (2012). Shallow axial magma chamber at the slow-spreading Erta Ale Ridge. *Nature Geoscience*, *5*(4), 284–288. https://doi.org/10.1038/ngeo1414

Pagli, C., Yun, S.-H., Ebinger, C., Keir, D., & Wang, H. (2019). Strike-slip tectonics during rift linkage. *Geology*, *47*(1), 31–34. https://doi.org/10.1130/g45345.1

Refice, A., Belmonte, A., Bovenga, F., & Pasquariello, G. (2011). On the use of anisotropic covariance models in estimating atmospheric DInSAR contributions. *IEEE Geoscience and Remote Sensing Letters*, *8*(2), 341–345. https://doi.org/10.1109/lgrs.2010.2073440

Ruegg, J., Briole, P., Feigl, K., Orsoni, A., Vigny, C., Abdallah, M. A., et al. (1993). First epoch geodetic GPS measurements across the Afar plate boundary zone. *Geophysical Research Letters*, *20*(18), 1899–1902. https://doi.org/10.1029/93gl01882

Ruegg, J., & Kasser, M. (1987). Deformation across the Asal-Ghoubbet rift, Djibouti, uplift and crustal extension 1979–1986. *Geophysical Research Letters*, *14*(7), 745–748. https://doi.org/10.1029/gl014i007p00745

Ruegg, J., & Pilger, A. (1975). Main results about the crustal and upper mantle structure of the Djibouti region (TFAI). *Afar Depression of Ethiopia*, *1*, 120–134.

Saria, E., Calais, E., Stamps, D. S., Delvaux, D., & Hartnady, C. J. (2014). Present-day kinematics of the East African Rift. *Journal of Geophysical Research: Solid Earth*, *119*, 3584–3600. https://doi.org/10.1002/2013JB010901

Schilling, J. (1973). Afar mantle plume: Rare earth evidence. *Nature Physical Science*, *242*(114), 2–5. https://doi.org/10.1038/physci242002a0

Schult, A. (1974). Palaeomagnetism of Tertiary volcanic rocks from the Ethiopian southern plateau and the Danakil block. *Journal of Geophysics*, *40*(1), 203–212.

Shen, L., Hooper, A., & Elliott, J. (2019). A spatially varying scaling method for InSAR tropospheric corrections using a high-resolution weather model. *Journal of Geophysical Research: Solid Earth*, *124*(4), 4051–4068. https://doi.org/10.1029/2018jb016189

Sigmundsson, F. (1992). Tectonic implications of the 1989 Afar earthquake sequence. *Geophysical Research Letters*, *19*(9), 877–880. https://doi.org/10.1029/92gl00686

Smittarello, D., Grandin, R., De Chabalier, J.-B., Doubre, C., Deprez, A., Masson, F., et al. (2016). Transient deformation in the Asal-Ghoubbet Rift (Djibouti) since the 1978 diking event: Is deformation controlled by magma supply rates? *Journal of Geophysical Research: Solid Earth*, *121*(8), 6030–6052. https://doi.org/10.1002/2016jb013069

Sousa, J. J., Hooper, A. J., Hanssen, R. F., Bastos, L. C., & Ruiz, A. M. (2011). Persistent Scatterer InSAR: A comparison of methodologies based on a model of temporal deformation vs. spatial correlation selection criteria. *Remote Sensing of Environment*, *115*(10), 2652–2663. https://doi.org/10.1016/j.rse.2011.05.021

Stork, A. L., Stuart, G. W., Henderson, C. M., Keir, D., & Hammond, J. O. (2013). Uppermost mantle (Pn) velocity model for the Afar region, Ethiopia: An insight into rifting processes. *Geophysical Journal International*, *193*, 321–328. https://doi.org/10.1093/gji/ggs106

Tapponnier, P., Armijo, R., Manighetti, I., & Courtillot, V. (1990). Bookshelf faulting and horizontal block rotations between overlapping rifts in southern Afar. *Geophysical Research Letters*, *17*(1), 1–4. https://doi.org/10.1029/gl017i001p00001

Tarantola, A., Ruegg, J. C., & Lepine, J. C. (1979). Geodetic evidence for rifting in Afar a brittle-elastic model of the behaviour of the lithosphere. *Earth and Planetary Science Letters*, *45*, 435–444. https://doi.org/10.1016/0012-821X(79)90142-0

Temtime, T. (2021). *Tectonic, volcanic and geothermal processes in a continental rift* (Unpublished doctoral dissertation). School of Earth Sciences, University of Bristol.

Temtime, T., Biggs, J., Lewi, E., Hamling, I., Wright, T., & Ayele, A. (2018). Spatial and temporal patterns of deformation at the Tendaho geothermal prospect, Ethiopia. *Journal of Volcanology and Geothermal Research*, *357*, 56–67. https://doi.org/10.1016/j.jvolgeores.2018.04.004

Tiberi, C., Ebinger, C., Ballu, V., Stuart, G., & Oluma, B. (2005). Inverse models of gravity data from the Red Sea-Aden-East African rifts triple junction zone. *Geophysical Journal International*, *163*, 775–787. https://doi.org/10.1111/j.1365-246X.2005.02736.x

Viltres, R., Jónsson, S., Ruch, J., Doubre, C., Reilinger, R., Floyd, M., & Ogubazghi, G. (2020). Kinematics and deformation of the southern Red Sea region from GPS observations. *Geophysical Journal International*, *221*(3), 2143–2154. https://doi.org/10.1093/gji/ggaa109

Wang, H., & Wright, T. (2012). Satellite geodetic imaging reveals internal deformation of western Tibet. *Geophysical Research Letters*, *39*(7). https://doi.org/10.1029/2012gl051222

Wang, H., Wright, T. J., Yu, Y., Lin, H., Jiang, L., Li, C., & Qiu, G. (2012). InSAR reveals coastal subsidence in the Pearl River Delta, China. *Geophysical Journal International*, *191*(3), 1119–1128. https://doi.org/10.1111/j.1365-246x.2012.05687.x

Weiss, J. R., Walters, R. J., Morishita, Y., Wright, T. J., Lazecky, M., Wang, H., et al. (2020). High-resolution surface velocities and strain for Anatolia from Sentinel-1 InSAR and GNSS data. *Geophysical Research Letters*, *47*(17), e2020GL087376. https://doi.org/10.1029/2020gl087376

Werner, C., Wegmuller, U., Strozzi, T., & Wiesmann, A. (2000). *GAMMA SAR and interferometric processing software* (Vol. 461, pp. 211–219). European Space Agency, (Special Publication) ESA SP.

White, R., & McKenzie, D. (1989). Magmatism at rift zones: The generation of volcanic continental margins and flood basalts. *Journal of Geophysical Research: Solid Earth*, *94*(B6), 7685–7729. https://doi.org/10.1029/jb094ib06p07685

Wiart, P., & Oppenheimer, C. (2000). Largest known historical eruption in Africa: Dubbi volcano, Eritrea, 1861. *Geology*, *28*(4), 291–294. https://doi.org/10.1130/0091-7613(2000)028<0291:lkheia>2.3.co;2

Wolfenden, E., Ebinger, C., Yirgu, G., Deino, A., & Ayalew, D. (2004). Evolution of the northern Main Ethiopian rift: Birth of a triple junction. *Earth and Planetary Science Letters*, *224*(1–2), 213–228. https://doi.org/10.1016/j.epsl.2004.04.022

Wright, T. J., Ebinger, C., Biggs, J., Ayele, A., Yirgu, G., Keir, D., & Stork, A. (2006). Magma-maintained rift segmentation at continental rupture in the 2005 Afar dyking episode. *Nature*, *442*(7100), 291–294. https://doi.org/10.1038/nature04978

Wright, T. J., Parsons, B. E., & Zhong, L. (2004). Toward mapping surface deformation in three dimensions using InSAR. *Geophysical Research Letters*, *31*(1). https://doi.org/10.1029/2003GL018827

Wright, T. J., Sigmundsson, F., Pagli, C., Belachew, M., Hamling, I. J., Brandsdóttir, B., et al. (2012). Geophysical constraints on the dynamics of spreading centres from rifting episodes on land. *Nature*, *5*(4), 242–250. https://doi.org/10.1038/ngeo1428

Xu, W., Rivalta, E., & Li, X. (2017). Magmatic architecture within a rift segment: Articulate axial magma storage at Erta Ale volcano, Ethiopia. *Earth and Planetary Science Letters*, *476*, 79–86. https://doi.org/10.1016/j.epsl.2017.07.051

Xu, W., Xie, L., Aoki, Y., Rivalta, E., & Jónsson, S. (2020). Volcano-wide deformation after the 2017 Erta Ale dike intrusion, Ethiopia, observed with radar interferometry. *Journal of Geophysical Research: Solid Earth*, *125*(8), e2020JB019562. https://doi.org/10.1029/2020jb019562

Yu, C., Li, Z., & Penna, N. T. (2018). Interferometric synthetic aperture radar atmospheric correction using a GPS-based iterative tropospheric decomposition model. *Remote Sensing of Environment*, *204*, 109–121. https://doi.org/10.1016/j.rse.2017.10.038

Yu, C., Penna, N. T., & Li, Z. (2017). Generation of real-time mode high-resolution water vapor fields from GPS observations. *Journal of Geophysical Research*, *122*(3), 2008–2025. https://doi.org/10.1002/2016JD025753